Supplementary Information (SI) for Nanoscale.
This journal is © The Royal Society of Chemistry 2026

Supplementary Information

Disentangling Melanin Self-Assembly *via* Nanoprecipitation: From Protoparticles to Supraparticles

Meera Madhu, Adithya Vaidyanathan, Bárbara Fornaciari, and Bern Kohler*

Department of Chemistry and Biochemistry, The Ohio State University, 100 West 18th Avenue, Columbus, Ohio 43210, USA

Table of Contents

S1. Fabricating supraparticles from protoparticles

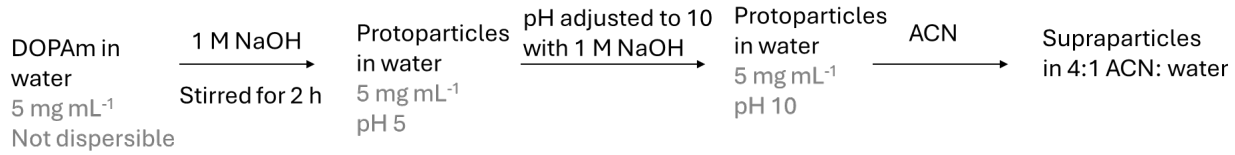

Scheme S1. Schematic illustrating the workflow for nanoprecipitation of protoparticles. DOPAm was dispersed in water by adjusting the pH to 8 with 1 M NaOH, followed by stirring for 2 hours. After stirring, the pH decreased to 5, which was then readjusted to 10 prior to the addition of acetonitrile (ACN).

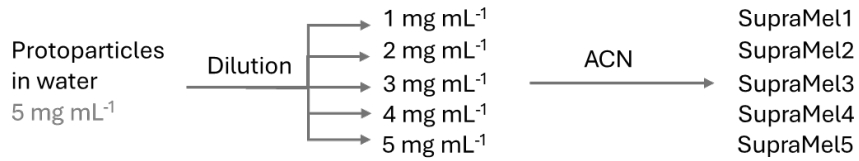

Scheme S2. Size control of the supraparticles by varying the concentration of the protoparticles in water prior to adding ACN. The pH of the initial 5 mg mL^{-1} dispersion was adjusted to pH 7.

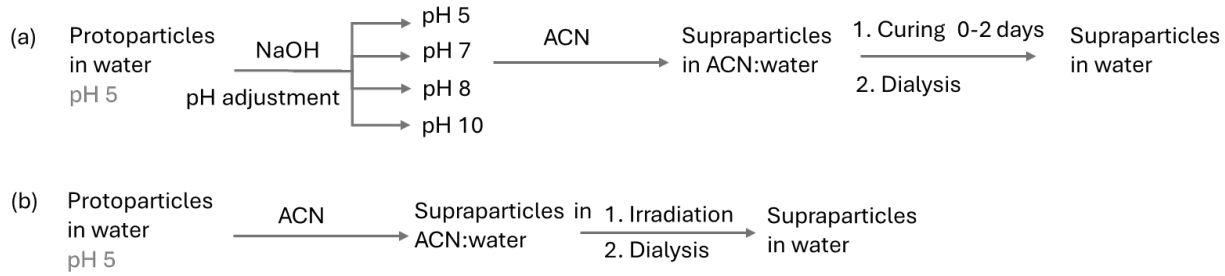

Scheme S3. (a) Workflow to investigate the effect of (a) initial pH of the aqueous protoparticle dispersion on the stability of the final supraparticles obtained after curing for a variable time followed by dialysis. (b) Workflow to study the effects of irradiation of the supraparticles in the ACN:water dispersion on stability against removal of ACN by dialysis. The initial concentrations of the protoparticles dispersions were fixed at 2 mg mL^{-1}.

S2. Viscosity and refractive index estimation of solvent mixtures

Following dilution of SupraMel0.5–5 stock dispersions with ACN to a standardized concentration of 0.1 mg mL^{-1}, the resulting solvent composition was 80% v/v ACN. Viscosity was calculated using the Arrhenius mixing rule:[1]

$$\ln \eta_{mix} = \sum_{i=1}^{N} x_i \ln \eta_i$$

where η_{mix}, x_i, η_i are the viscosity of the mixture, mole fraction and the viscosity of component *i*, respectively. The viscosities of the pure solvents at 25°C were taken as 0.887 cP for water and 0.334 cP for acetonitrile. 0.776 g mL^{-1} was used as the density of acetonitrile and 0.997 mg mL^{-1} was used for water. Viscosity was estimated to be 0.50 cP for 80% v/v ACN.

The refractive index of each dispersion was estimated using the Arago-Biot model:[2]

$$n_{mix} = \phi_1 n_1 + \phi_2 n_2$$

where n_{mix}, ϕ_i, n_i are the refractive index of the mixture, volume fraction of each solvent and the refractive index of the pure solvents, respectively. The refractive indices of water and acetonitrile were taken to be 1.33 and 1.34, respectively. The estimated refractive index of the 80% v/v acetonitrile was estimated to be 1.34, which is the same as pure acetonitrile.

S3. DLS measurements and data processing

DLS measurements were performed on 0.1 mg mL^{-1} dispersions with an absorbance of 0.4 at 633 nm unless otherwise specified. This concentration is high compared to earlier DLS studies on DOPA melanin,[3,4] but was necessary in our case to obtained measured count rates of scattered photons greater than 2×10^5 s^{-1} for all samples. The Zetasizer Pro instrument used here uses a backscatter configuration and the optimal position within the sample cell is automatically determined by the instrument such that effects of multiple scattering or absorbance are minimized, compared to instruments that utilize a 90° detection geometry. Data was collected

and analyzed using the Zetasizer Nano software. Data quality was assessed using the derived count rate, which represents the measured photon count rate corrected for the attenuator automatically selected by the instrument to maintain a measured count rate between (2–5) × 10^5 s^{-1}. For samples exhibiting irregular or unstable aggregation, the autocorrelation functions (ACFs) deviated from the expected smooth exponential decay. In these cases, raw ACFs are included and discussed, as standard fitting algorithms were not reliable due to signal-to-noise considerations. Intensity-weighted size distributions and average sizes are presented only when three consecutive runs yielded consistent size distributions.

Z-average sizes and the polydispersity index (PDI) were determined using the cumulants analysis method. This method fits the ACF to a single exponential decay up to 10% of the y-intercept. The sizes reported for the supraparticles in the main text are *Z*-average sizes as cumulants analysis is the standard method recommended by ISO 13321:1996 and ISO 22412:2017 standards.

PDI, which provides a measure of the width of the particle size distribution, is defined as

$$\mathrm{PDI} = \left(\frac{\sigma}{Z}\right)^2, \tag{S1}$$

where σ is the standard deviation of a gaussian distribution centered around Z (Z-average). PDIs for the size-controlled particles are given in Table S2. It serves as a standard metric to assess dispersity, with values below 0.1 typically considered indicative of monodisperse samples.[5]

The intensity-weighted size distributions reported were obtained using the general-purpose analysis algorithm provided by the Zetasizer software. This algorithm fits the measured

ACF up to 1% of the *y*–intercept. As such, it is sensitive to the presence of larger particles and better reflects the full distribution of particle sizes in heterogeneous samples. Compared to the cumulants analysis, which force-fits the ACF to a single exponential, the general purpose algorithm does not make any assumptions about different sized particle populations, making it more appropriate for samples of unknown polydispersity. Average particle sizes from these distributions are reported in Table S2 for the size-controlled particles. The *Z*-average diameters and average peak sizes are in close agreement for the nanoprecipitated samples, highlighting their monodisperse nature. The values are reported in Table S1, S2 with an error bar of ±2σ, where σ is the standard deviation of the mean value calculated from the three replicates.

S4. AFM image processing

AFM images were processed and analyzed using Nanoscope Analysis 3.0. The images were corrected for tilt by applying a first-order polynomial correction along each horizontal line scan. To analyze the average particle height and diameter from the images, the 'Particle Analysis' command was used. Features of interest were selected by setting a threshold value to include only pixels above a specified height. Particles touching the image boundaries were excluded from the analysis of SupraMel images. Additionally, aggregates of supraparticles were manually excluded from diameter measurements. In SupraMel samples with particles of different sizes, populations of each size were selected individually by selecting pixels with heights between a lower and higher threshold values. The mass percentage of distinct particle populations was calculated based on their relative volumes (projected area × average height), assuming equal

density across all size fractions. The average diameters of the supraparticles are reported along with 2σ (standard deviation) errors.

To estimate the actual lateral size of the protoparticles, corrections for AFM tip convolution effects were applied following the procedure of Canet-Ferrer et al.[6] The nominal radius of the AFM tip (2 nm) was used to calculate the lower limit of lateral broadening. When the particle height (h) is smaller than the tip radius (r_{tip}), as is the case here, the convolution error (2Δ) that should be subtracted from the apparent diameter to obtain the deconvoluted diameter is estimated from,

$$2\Delta = 2r_{\mathrm{tip}} \cos\left\{\sin^{-1}\left[\frac{r_{\mathrm{tip}}-h}{r_{\mathrm{tip}}}\right]\right\}. \quad \text{(S1)}$$

Using $h = 1.3$ nm and $r_{\mathrm{tip}} = 2$ nm, 2Δ was estimated to be 3.7 nm. The smallest protoparticles measured by AFM have diameters approaching 5 nm, which suggests that their actual size after accounting for the finite size of the tip is approximately 2 nm.

S5. Supporting information tables and figures

Table S1. DLS derived mean count rate for DOPAm aqueous dispersions as a function of concentration.

Concentration of DOPAm / mg mL^{-1}	Derived count rate / 10^3 s^{-1}
0 (water only)	24 ± 5
0.1	93 ± 10
0.5	124 ± 17
1	131 ± 40
2	76 ± 18
3	45 ± 26

Table S2. Summary of DLS measurements of SupraMel-A particles prepared from initial protoparticle dispersions at pH 7.

Sample	Z-average / nm	PDI[a]	Average size / nm	Derived count rate / 10^3 s^{-1}
SupraMel1-A	33.2 ± 1.2	0.12 ± 0.03	34.2 ± 2.2	680 ± 6
SupraMel2-A	40 ± 3	0.10 ± 0.05	43 ± 3	1261 ± 20
SupraMel3-A	52.8 ± 1.0	0.08 ± 0.01	58 ± 3	7603 ± 10
SupraMel4-A	84.6 ± 1.8	0.10 ± 0.02	93 ± 6	(1.54 ± 0.16) × 10^4
SupraMel5-A	88.4 ± 3	0.14 ± 0.03	99 ± 5	(2.21 ± 0.19) × 10^4

[a] Polydispersity Index

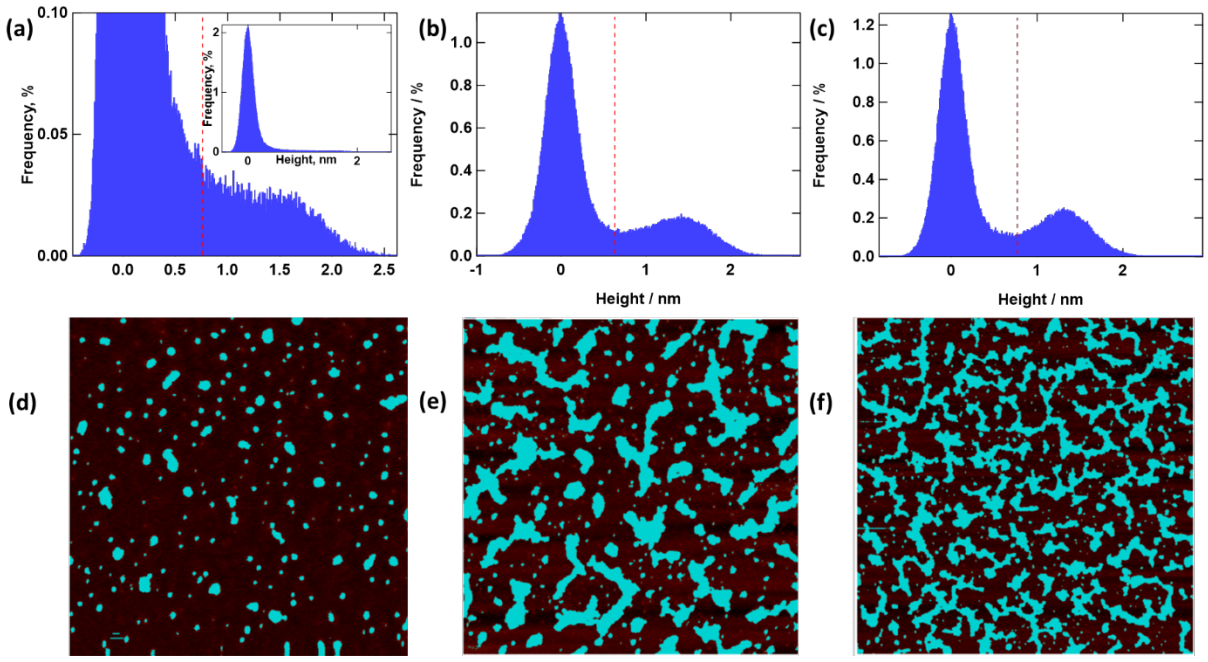

Figure S1. Height distributions of DOPAm drop-cast on mica from a dispersion with concentration of (a) 5, (b) 10, and (c) 30 μg mL^{-1}. The prominent peak near 0 nm corresponds to the bare mica substrate. In (a), a magnified view along the y-axis is plotted to highlight the height distribution attributed to the DOPAm particles. The inset shows the complete view. A threshold height of 0.632 nm (indicated by the red dashed line in (a)–(c) was used to distinguish DOPAm particles from the substrate. AFM images in (d)–(f) show pixels corresponding to heights above this threshold, highlighting the spatial distribution of DOPAm at 5, 10, and 30 μg mL^{-1}, respectively. The average particle height at each concentration was calculated using a weighted average of the height distribution above the threshold. The average height of DOPAm drop casted at 5, 10, and 30 μg mL^{-1} are 1.2 ± 0.4 nm, 1.3 ± 0.4 nm, and 1.2 ± 0.1 nm, respectively.

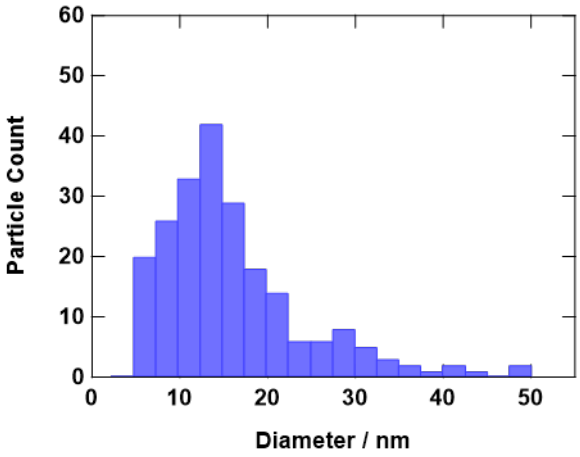

Figure S2. Distribution of diameters of the particles in Fig. 2(a), which are highlighted in Figure S1(d). The diameter corresponds to circles with the same area as the highlighted features.

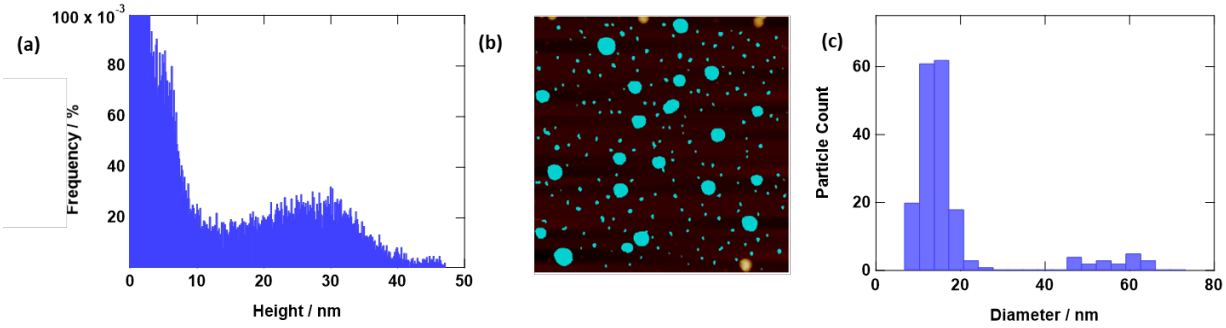

Figure S3. (a) Histogram showing the height of every pixel in the AFM image of SupraMel2-A presented in Figure 3b. The number of bins was set to 512. (b) Particles selected for analyzing the diameter distribution. Cyan highlights indicate regions where the measured height exceeded the 0.4 nm threshold. (c) Distribution of the diameters of the particles highlighted in cyan in (b).

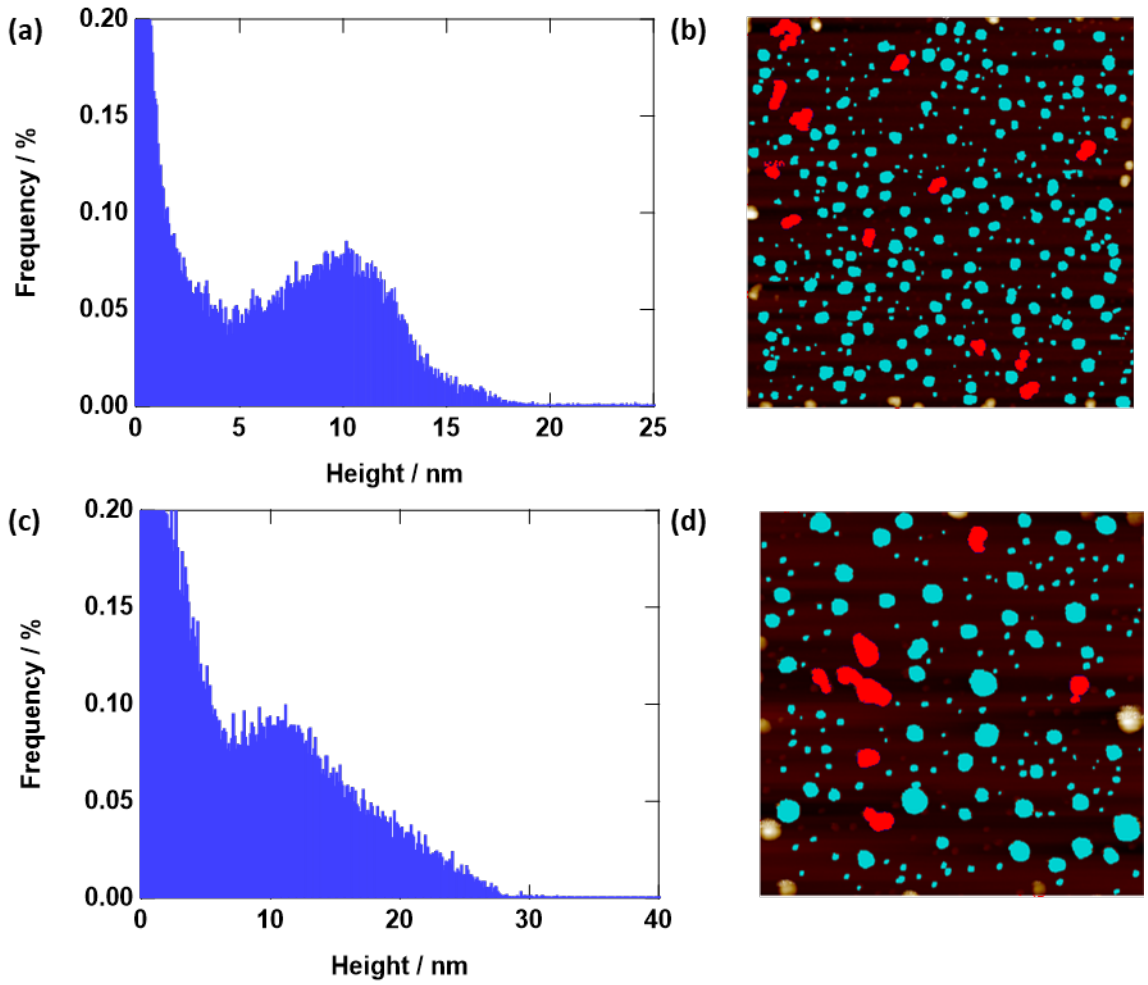

Figure S4. Particle size analysis corresponding to AFM images of SupraMel1-A and SupraMel3-A in Figure 4c, d. Panels a-b show results for SupraMel1 and panels c-d show results for SupraMel3. (a, c) Height distribution, and (b, d) particles selected for lateral size analysis. The cyan shading in (b) and (d) indicate regions where the measured height exceeds a threshold of 0.2 nm or 0.3 nm, respectively. Supraparticles in contact with other supraparticles are highlighted in red and were excluded from the analysis.

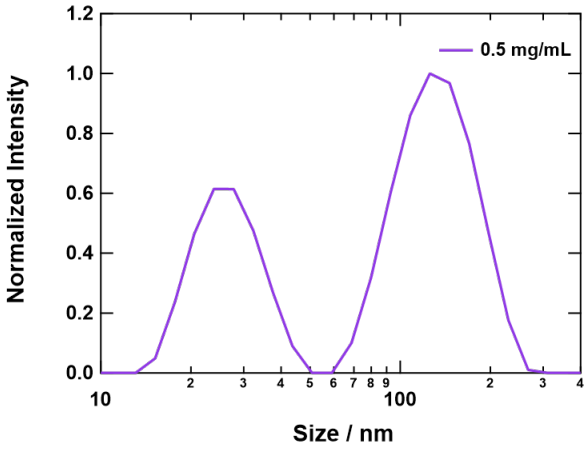

Figure S5. Normalized intensity distribution from DLS for SupraMel0.5-A, showing a bimodal size distribution with peaks centered at 27.2 ± 1.5 nm and 131 ± 13 nm, corresponding to the smaller and larger particle populations, respectively.

S6. Stability of SupraMel particles in water

The stability of dialyzed SupraMel2 particles was evaluated under different physical stress conditions. To assess the effect of aging in water, a 0.1 mg mL^{-1} aqueous dispersion of SupraMel2 was stored in a glass vial at room temperature in the dark. Aliquots were taken at 0, 24, 48, and 72 hours after dialysis and analyzed using DLS.

To further test the stability of the supraparticles in water, fresh aliquots of the dialyzed SupraMel2 dispersions (0.4 mg mL^{-1}) were placed in glass vials and subjected to ultrasonic agitation in a bath sonicator for 10 minutes. For thermal stability, an aliquot of dialyzed SupraMel2 (10 mL, 0.4 mg mL^{-1}) was refluxed at 80 °C for 24 h with continuous stirring in a round-bottom flask. In all cases, particle size distributions were evaluated by DLS following treatment to assess any changes in the size distribution.

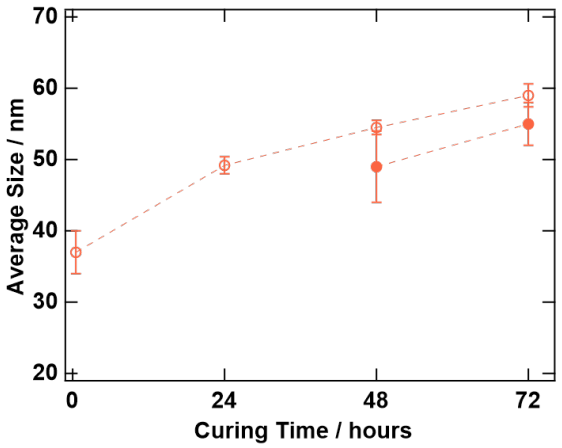

Figure S6. Effect of curing time on supraparticle stability. Average hydrodynamic diameter from DLS measurements of supraparticles prepared from 2 mg mL^{-1} DOPAm dispersions (pH 7). Open circles are measured for SupraMel-A particles in 80% acetonitrile before dialysis, and filled circles represent the size of the SupraMel particles in water after dialysis. The absence of a filled circle indicates that stable supraparticles were not observed after dialysis.

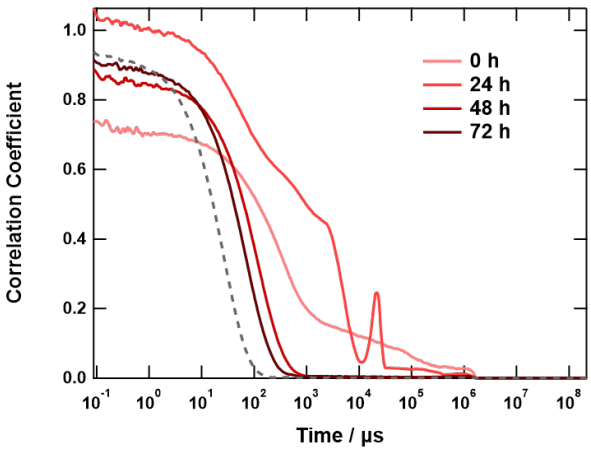

Figure S7. ACFs of dialyzed SupraMel2 after different curing times. The ACF of the supraparticles in acetonitrile:water mixed solvent without any curing is shown by the gray dashed line. The dialyzed samples that did not cure for sufficiently long times exhibit *y*-intercepts > 1, discontinuities and elevated baselines at longer times.

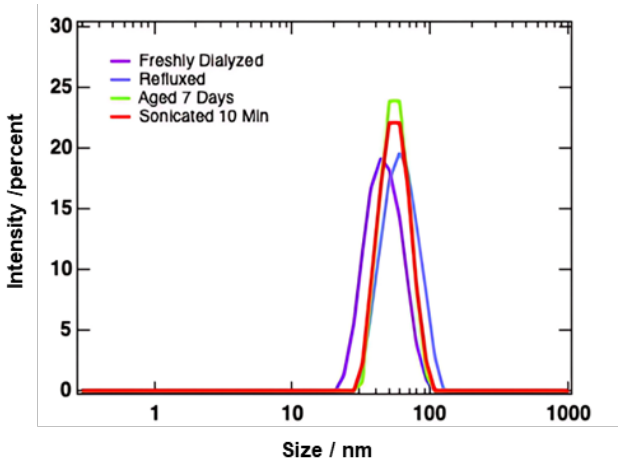

Figure S8. Stability testing of SupraMel2 supraparticles nanoprecipitated from a pH 10 aqueous dispersion. Intensity-weighted hydrodynamic size distributions obtained by DLS are compared for aliquots of freshly dialyzed sample (purple, average hydrodynamic diameter 47.8 ± 2.2 nm), an aliquot that was refluxed 24 h at 80 °C (blue, 62.7 ± 2.3 nm), an aliquot that was aged 7 days at room temperature in the dark (green, 56 ± 3 nm), and an aliquot that was sonicated for 10 min (red, 56 ± 3 nm) 0.3 mg mL^{-1} dispersions. Each trace shows a single, narrow peak, indicating that aging, thermal, and mechanical stresses minimally impact supraparticle size or polydispersity within this 50–65 nm size range.

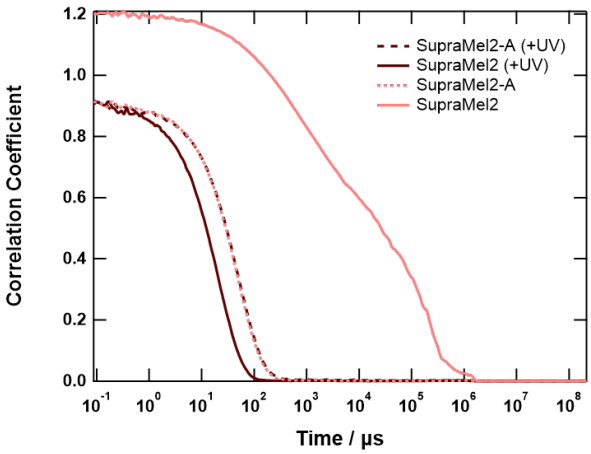

Figure S9. ACF from DLS measurements of SupraMel2 supraparticles prepared at initial pH 5, comparing irradiated and non-irradiated samples. Measurements from samples before and after dialysis are plotted as dashed and solid lines, respectively. The sample that was not irradiated prior to dialysis (pale red solid line) exhibits a *y*-intercept that exceeds unity and elevated baseline, indicating that a very broad distribution of particles is present. In contrast, the irradiated sample (dark solid red line) exhibits a smooth ACF curve, as generally seen for uniform particles.

S7. References

(1) Arrhenius, S. Über die innere Reibung verdünnter wässeriger Lösungen. *Z. Für Phys. Chem.* **1887**, *1U* (1), 285–298. https://doi.org/10.1515/zpch-1887-0133.

(2) Reis, J. C. R.; Lampreia, I. M. S.; Santos, Â. F. S.; Moita, M. L. C. J.; Douhéret, G. Refractive Index of Liquid Mixtures: Theory and Experiment. *ChemPhysChem* **2010**, *11* (17), 3722–3733. https://doi.org/10.1002/cphc.201000566.

(3) Chen, Y.; Kendall, T.; Yip, P.; Davy, A.; Sefcik, J.; Sutter, J. U. Influence of Ions and pH on the Formation of Solid- and Liquid-like Melanin. *ACS Omega* **2020**, *5* (39), 25059–25068. https://doi.org/10.1021/acsomega.0c01953.

(4) Huang, J. S.; Sung, J.; Eisner, M.; Moss, S. C.; Gallas, J. The Fractal Structure and the Dynamics of Aggregation of Synthetic Melanin in Low *p* H Aqueous Solutions. *J. Chem. Phys.* **1989**, *90* (1), 25–29. https://doi.org/10.1063/1.456528.

(5) Takechi-Haraya, Y.; Ohgita, T.; Demizu, Y.; Saito, H.; Izutsu, K.; Sakai-Kato, K. Current Status and Challenges of Analytical Methods for Evaluation of Size and Surface Modification of Nanoparticle-Based Drug Formulations. *AAPS PharmSciTech* **2022**, *23* (5), 150. https://doi.org/10.1208/s12249-022-02303-y.

(6) Canet-Ferrer, J.; Coronado, E.; Forment-Aliaga, A.; Pinilla-Cienfuegos, E. Correction of the Tip Convolution Effects in the Imaging of Nanostructures Studied through Scanning Force Microscopy. *Nanotechnology* **2014**, *25* (39), 395703. https://doi.org/10.1088/0957-4484/25/39/395703.